

# Optimizing spin-based terahertz emission from magnetic heterostructures

Francesco Foggetti,\* Francesco Cosco,† and Peter M. Oppeneer

*Department of Physics and Astronomy, P. O. Box 516, Uppsala University, SE-75120 Uppsala, Sweden*

Henri Jaffrè

*Laboratoire Albert Fert, CNRS, Thales, Université Paris-Saclay, F-91767 Palaiseau, France*

Niloufar Nilforoushan, Juliette Mangeney, and Sukhdeep Dhillon

*Laboratoire de Physique de l'Ecole Normale Supérieure, ENS, Université PSL,*

*CNRS, Sorbonne Université, Université Paris Cité, F-75005 Paris, France*

(Dated: February 2, 2026)

Terahertz radiation pulses can be generated efficiently through femtosecond laser excitation of a ferromagnetic/nonmagnetic heterostructure, wherein an ultrafast laser-induced spin current results in an electromagnetic THz pulse due to spin-charge conversion. It is, however, still poorly understood how the THz emission amplitude and its bandwidth in the frequency regime can be optimized. Here, we perform a systematic analysis of the THz emission from various magnetic heterostructures. The dynamics of the spin current is described by the semiclassical, superdiffusive spin-transport model and the energy dependence of the spin Hall effect of hot electrons is taken into account, leading to emission profiles for Co(2 nm)/Pt(4 nm) bilayer in good agreement with experiment. To identify the optimal conditions for THz emission, we study the properties of the emitted THz wave profile by systematically varying the layer thicknesses of metallic bilayers, their interfacial spin-current transmission properties, their materials' dependence, and influence of the pump laser-pulse width, allowing us to give optimization guidelines. We find that thin nonmagnetic layer thicknesses of 5–6 nm provide the largest bandwidth in the case of Co/Pt and that the peak frequency of the THz emission depends only on the geometry of the emitter and not on the laser pulse width. The THz bandwidth is conversely found to depend on several factors such as exciting laser pulse width, layers' thicknesses, and interface transmission-reflection properties, with the limitation that an increase in the bandwidth by tuning the interface properties comes with a trade-off in the energy efficiency of the emitter. Lastly, we propose a double pulse excitation protocol of a trilayer system that could provide broadband THz emission with a large bandwidth. Our results contribute to establishing guidelines for optimizing spintronic THz generation.

## I. INTRODUCTION

The terahertz frequency band is positioned between the gigahertz frequency of electronics and the infrared frequency range of optics [1–3]. THz radiation was previously difficult to generate, but in the last decades various THz sources have been developed [4–8]. The most widely used THz emitters, based on THz emission from nonlinear semiconductor crystals via optical rectification or photoconductive antennas [1, 4, 6, 9, 10], suffer from limited bandwidth capabilities.

Spin-based THz emitters, discovered a decade ago, provide a technology framework that can overcome this limitation [11–14]. The basic principle of this technology involves exciting the magnetization of a nanometer-thick heterostructure via a femtosecond laser pulse which triggers an ultrafast demagnetization process of the ferromagnetic (FM) layer, as depicted in Fig. 1. The demagnetization is associated with the generation of a spin current which is injected into a nonmagnetic (NM) metal.

In the NM layer the spin current burst is converted in a transverse charge current through spin-to-charge conversion processes that lead to the efficient generation of a THz radiation pulse [11, 15–19]. The generated short transverse charge current causes emission of electromagnetic radiation in the THz regime through electric dipole emission [15, 20]. The spin-to-charge conversion in the NM material, which is typically a heavy metal, occurs through the inverse spin Hall effect (ISHE) [21, 22], which is a relativistic effect, caused by the spin-orbit interaction [23]. A further important role in the spin-to-charge conversion is played by the inverse Rashba-Edelstein effect (REE) [24, 25], in particular for ultrathin systems where the contribution of Rashba interfaces to THz emission can be comparable or greater than the contribution of ISHE which is a bulk effect [26–28].

Although the basic principle of the THz emission is mostly accepted, there remain several open questions. One of these is the proportionality of the THz electric field to the generating source. Different proportionality behaviors have been proposed, such as  $E \propto J_c$ , or  $\partial J_c / \partial t$ , or  $\partial^2 M / \partial t^2$ , and  $\partial M / \partial t$ , where  $J_c$  is the charge current and  $M$  is the magnetization of the FM layer, see Refs. [11, 29–38] and references therein. A further important question is, what properties of the metallic bilayer determine the THz emission, and how these properties can be

\* francesco.foggetti@physics.uu.se

† Present address: VTT Technical Research Center, Espoo, Finland

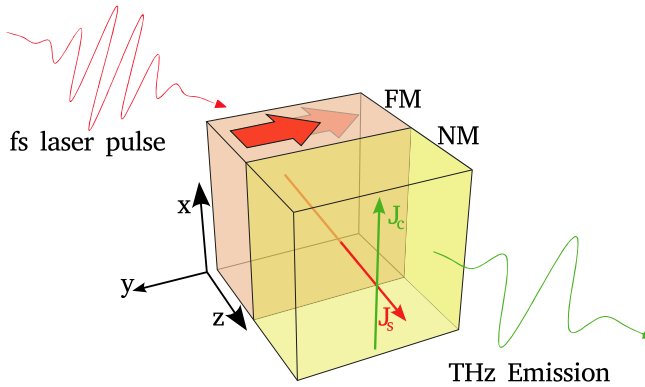


FIG. 1. Pictorial representation of a spin-based THz emitter. The fs laser pulse excites the ferromagnetic (FM) layer, reducing the magnetization and generating a longitudinal spin current, which is converted to a charge current in the non-magnetic (NM) layer via the inverse spin Hall effect. The resulting time-varying transverse charge current is the source for the THz pulse emission.

tuned to maximize THz emission signal.

In this work we address the latter question, through theoretical modeling of the THz pulse generation and the THz wave shape. Our main aim is to understand the factors that influence the THz emission and to provide guidelines for achieving the maximal THz electric field at a peak frequency  $\nu_{\max}$  as well as generating a THz emission spectrum that has a high bandwidth. This kind of modeling is relevant, as control over the THz frequency band of the electromagnetic spectrum is generally believed to promise rich opportunities for the technological advancement of many fields such as spectral imaging, industrial quality control, high-speed electronics, medical diagnostics, and telecommunications [1–3, 5, 39, 40].

Here, we systematically study the THz emission caused by superdiffusive spin currents that are generated by pulsed laser excitation in the FM layer and that rapidly penetrate the NM layer (Fig. 1) [15, 41–43]. In Sec. II, we introduce the theoretical methodology on which we base our analysis, the superdiffusion spin-transport model [41, 42, 44–47]. This model provides an accurate description of ultrafast demagnetization processes in magnetic heterostructures [15, 48–51]. We then describe how to apply the formalism to obtain the laser-induced spin currents responsible for the THz emission.

In Sec. III we report the main results of this paper. First, we start with comparing our model simulations with experimental THz emission data of a Co(2 nm)/Pt(4 nm) bilayer in Sec. III A, resulting in a very good agreement. Subsequently, we adopt the bilayer geometry of the FM/NM type in the following parts of Sec. III. We show how the femtosecond laser pulse features, such as pulse duration, influence the THz emission. Then, we characterize the THz spectrum according to the characteristics of the sample, such as the relative thickness of the layers

(in the Appendix A we report results for different FM materials). Furthermore, we study the role of interface properties in the THz emission, by varying the reflection properties of the emitter at the central interface, i.e. between the FM and NM layer, and at the outer interfaces, between the emitter and outside. Finally, in Sec. III G we propose a novel kind of setup, a FM/NM/FM trilayer which is excited from both the FM sides by two separate laser pulses with a well defined time delay, which causes interference of the spin currents in the emitter and results in a larger bandwidth profile.

## II. METHODOLOGY

The superdiffusive spin transport model [41, 44, 45, 47] has been developed to describe in a simple and intuitive fashion the ultrafast laser-induced demagnetization in layered heterostructures of the type FM/NM. In the key idea of the model, a femtosecond laser pulse exciting a ferromagnetic material creates energetic spin-polarized electrons that have anomalous transport characteristics. Hot spin majority and minority electrons have different spectral properties, specifically, they move in the sample at different speeds and have different lifetimes [52–54]. These differences give rise to a spin-polarized diffusion which is responsible for the demagnetization of the ferromagnetic layer as the induced, longitudinal spin current leaves the magnetic layer and is injected in the nonmagnetic material, see Fig. 1.

In our study, a laser pulse initiates the electronic transport by exciting electrons with energies at and below the Fermi level – typically occupying strongly *d*-hybridized and relatively immobile states – into higher energy bands of *sp* character. These *sp* electrons are characterized by higher velocities, hence, they behave as itinerant particles moving through the sample [55]. We note that an alternative approach to describe the collision-rich motion of excited hot electrons in metallic layers has been developed on the basis of Boltzmann transport theory [56, 57].

The superdiffusive transport model describes two spin channels, tagged as  $\sigma \in \{\uparrow, \downarrow\}$ , for the electronic transport. Each spin channel is characterized by the hot electron velocities,  $v_\sigma(\epsilon)$ , and lifetimes,  $\tau_\sigma(\epsilon, z)$ , which depend on the electron energy  $\epsilon$ , and, in magnetic materials, on the spin  $\sigma$  as well. The lifetime  $\tau$  is a  $z$ -dependent quantity due to the layered structure of the emitter, wherein different materials along  $z$  have different lifetimes. Because of the distinct transport properties of the two spin channels, the current of hot electrons becomes spin polarized in the magnetic layer. In addition, in the case of multilayers, spin filtering via multiple spin-dependent transmissions and reflections at the interfaces further contributes to the spin polarization of the current [55].

The outflow of the spin-polarized current  $J_s$  initiated by a laser pulse results in a loss of local magnetic momentum and corresponding demagnetization  $dM/dt$ . Due

to the high velocities of hot electrons, the demagnetization happens typically on the timescale of a few hundred femtoseconds [44]. In the superdiffusive model the hot electrons propagate initially ballistically in approximately the first 100 fs. However, due to the relaxation processes caused by electron scattering and thermalization, the hot electron transport continuously changes its character. In about 500 fs up to 1 ps it develops into diffusive transport. In the time interval up to 500 fs, the transport proceeds in the superdiffusive regime [41].

Let us describe briefly the main features of the superdiffusive spin-dependent transport model, which revolves around the equation of motion for the hot electron density  $n_\sigma(\epsilon, z, t)$ , with spin  $\sigma$ , energy  $\epsilon$ , and position  $z$ ,

$$\frac{\partial n_\sigma(\epsilon, z, t)}{\partial t} + \frac{n_\sigma(\epsilon, z, t)}{\tau_\sigma(\epsilon, z)} = \left( -\frac{\partial}{\partial z} \hat{\phi} + \hat{I} \right) S_\sigma^{\text{eff}}(\epsilon, z, t), \quad (1)$$

where  $\hat{\phi}$  is the flux operator which contains the dependence from the electrons' velocities and describes interlayer transmissions and reflections. Furthermore,  $S_\sigma^{\text{eff}}(\epsilon, z, t)$  is an effective source term describing the laser induced excitation of spin-polarized hot electrons and scattering events within the material. It consists of two contributions,

$$S_\sigma^{\text{eff}}(\epsilon, z, t) = S_\sigma^{\text{ext}}(\epsilon, z, t) + S_\sigma^{\text{p}}(\epsilon, z, t), \quad (2)$$

where  $S_\sigma^{\text{ext}}(\epsilon, z, t)$  describes the excitation of hot electrons by the laser pulse, and  $S_\sigma^{\text{p}}(\epsilon, z, t)$  is the term describing the effects of scattering, mostly caused by electron-electron interactions, calculated as

$$S_\sigma^{\text{p}}(\epsilon, z, t + \delta t) = \sum_{\sigma'} \int_{\epsilon_{\text{Fermi}}}^{\epsilon_{\text{max}}} d\epsilon' n_{\sigma'}(\epsilon', z, t) \times p_{\sigma', \sigma}(\epsilon', \epsilon, z, t) \left( 1 - e^{-\delta t / \tau_{\sigma'}(\epsilon', z, t)} \right). \quad (3)$$

$p_{\sigma', \sigma}(\epsilon', \epsilon, z, t)$  is the probability that an electron at energy level  $\epsilon'$ , between the Fermi energy  $\epsilon_{\text{Fermi}}$  and the energy cut-off  $\epsilon_{\text{max}}$ , and spin  $\sigma'$  will move to energy level  $\epsilon$  with spin  $\sigma$  in the next time step,  $t + \delta t$ . Eq. (3) includes both the contributions from the scattered hot electrons, formally treated as newly excited, and the ones actually excited as the result of the scattering. For practical calculations we adopt the discretized version of the formalism, described in Ref. [55], with the space divided into computational cells of width  $\delta z$ . Time and energy are also sampled in finite steps of  $\delta t$  and  $\delta \epsilon$ , respectively. In this article, we use the spatial discretization step  $\delta z = 1$  nm, time step  $\delta t = 1$  fs, and energy step  $\delta \epsilon = 0.125$  eV.

When treating the multilayers, one should include the possibility of scattering at the interlayer interfaces. This is done by employing positions on the left and right-hand side of the interface,  $z_i^\pm = z_i \pm \delta z/2$ , for an interface centered at  $z_i$ , and computing the fluxes  $\vec{\Phi}_\sigma(z_i^\pm, t)$  and  $\vec{\Phi}_\sigma(z_i^\pm, t)$  of right and left moving particles, respectively, with spin  $\sigma$  that go through the interface  $z_i^\pm$  at time

$t$ . Each interface is characterized by spin and energy-dependent transmission or reflection coefficients for electrons moving to the right, or to the left, that can be obtained from first-principles calculations [19, 47, 55, 58].

The solution of the discretized version of Eq. (1) gives automatically access to the spin current density, defined as the difference between spin-up ( $\uparrow$ ) and spin-down ( $\downarrow$ ) electron flux densities flowing in and out ( $\rightarrow, \leftarrow$ ) at each point in space, i.e.,

$$J_s(z, t) = \frac{\hbar}{2} \left[ \vec{\Phi}_\uparrow(z, t) - \vec{\Phi}_\uparrow(z, t) - \vec{\Phi}_\downarrow(z, t) + \vec{\Phi}_\downarrow(z, t) \right]. \quad (4)$$

The spin current is converted via ISHE into a transient charge current as  $\mathbf{J}_c(z, t) = \frac{2e}{\hbar} \theta_{\text{SH}} \mathbf{J}_s(z, t) \times \mathbf{M} / |\mathbf{M}|$ , where  $\theta_{\text{SH}}$  is the spin Hall angle, and represents the efficiency of the spin-to-charge conversion process, and  $\mathbf{M}$  is the magnetization of the FM layer.

An important remark has to be made at this point, namely, that the spin Hall angle is energy dependent. It is defined as  $\theta_{\text{SH}} = \sigma_{\text{SH}} / \sigma$ , where  $\sigma_{\text{SH}}$  is the spin Hall conductivity and  $\sigma$  is the usual conductivity of the material [59]. In particular, the spin Hall conductivity will depend on the energy of hot electrons [60]. Due to the large spin-orbit interaction in Pt, a sizeable spin-charge conversion is obtained in spintronic emitters, making Pt a standard choice for the heavy-metal to realize high-amplitude spintronic emitters [7, 11, 13, 19, 61–63]. The energy-dependent spin Hall conductivity of Pt is large for hot electron energies close to the Fermi energy, but drops significantly for energies higher than 0.5 eV. The origin of this energy dependence is the 5d band structure of Pt, in which the top of the 5d band lies about 0.5 eV above the Fermi energy. Hot electrons with higher energies are injected into the Pt *sp* band, but the predicted spin Hall conductance for these electrons is much smaller. This means that hot electrons injected in the Pt layer will contribute differently to the emission, in particular, electrons with higher energy first need to lose energy, i.e., by scattering and decaying into lower energy levels, in order to give a significant contribution to the THz emission. As outlined recently, the contributions to the spin-to-charge conversion from the different hot-electron energy levels can be incorporated in the superdiffusive transport, see Ref. [64] for details. This renders the spin and charge currents to be disproportional. In the following simulations of spintronic THz emission, we include the energy dependence of the ISHE when we numerically compute the charge current.

Lastly, the time-varying charge current is responsible for the emitted THz signal. It has been discussed recently whether the emitted THz electric field would be proportional to the charge current  $J_c$  [11, 32, 65] or the time derivative of the charge current,  $\partial J_c / \partial t$  [33, 38, 66]. Although according to the Maxwell equations the electric amplitude in the far field should be proportional to  $\partial J_c / \partial t$  [67], the parabolic mirror used in the focusing optics of the THz detection leads to an effective time in-

tegration so that, in the frequency domain, one obtains [64]

$$E(\nu) \propto \int dz J_c(z, \nu). \quad (5)$$

This proportionality will be employed in the following simulations for the THz electric field from spintronic emitters.

### III. RESULTS

#### A. Comparison with experiment

Before delving into the possibilities to optimize the spintronic THz emission from spintronic heterostructures, we first compare the emission calculated with our methodology with measured THz emission, to examine how well the theoretical model is able to describe the experiment. Specifically, we consider a realistic Co/Pt heterostructure and we compare our modeling results with the measured THz spectrum emitted from a Co(2)/Pt(4) bilayer. Here and in the following, the numbers in parenthesis refer to the layer width in nm. A laser pulse of wavelength 1030 nm (1.2 eV) and width  $\tau_{\text{pulse}} = 23$  fs from an amplified laser system excites a hot spin-polarized current in the Co film and injects it in the Pt, where it is converted into a charge current that results in the THz pulsed emission. A THz-time domain spectroscopy setup is used to detect the amplitude and phase of the emitted THz pulse. For ultra-broadband detection a 20  $\mu\text{m}$  thick ZnTe crystal is employed for electro-optic sampling of the generated THz pulse [68, 69].

To compute the THz emission we employ the superdiffusion model in combination with spin-dependent electron lifetimes and velocities as given by first-principles calculations [53, 54]. Here, the external boundaries of the heterostructure, representing the capping material and substrate that enclose the emitter, are considered completely reflective ( $R=1$ ), because the measured sample was capped with  $\text{AlO}_x$  and prepared on a sapphire substrate. In order to estimate the reflection coefficients at the Co/Pt interface, we use the reflection coefficients reported in Ref. [58], where, however, only the reflection coefficients for Fe and Ni are presented. Thus, we decide to approximate the coefficients for Co as an average of these two. Furthermore, we take the energy dependence of the spin Hall conductivity and the response function of the 20- $\mu\text{m}$  ZnTe detector crystal into account (see [64]) as well as the integrating influence of the focusing mirror.

Figure 2 shows the simulated emission profile compared with the experimental data for a Co(2)/Pt(4) spintronic THz emitter.

The simulated THz emission spectrum is in good agreement with the experimental data: the frequency position of the emission peak is correctly predicted and the bandwidth is also in good agreement.

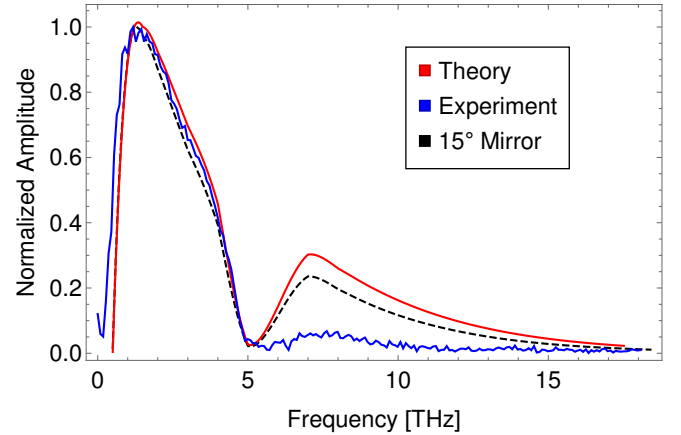


FIG. 2. Comparison of our modeling (red) and experiment (blue) for the THz amplitude spectrum of a Co(2 nm)/Pt(4 nm) emitter. The response function of the ZnTe detector is taken into account and is responsible for the dip at 5 THz. The THz emission amplitude  $E$  is normalized to its maximum value. The black-dashed line shows the theoretical emission accounting for a 15°-tilt of the parabolic detection mirror with respect to the propagation direction of the THz radiation.

The secondary peak that appears in Fig. 2 at 7–8 THz is related to the response function of the ZnTe detector, which has a dip at 5 THz. Such a peak is present, too, in the experimental data, although smaller in amplitude. Our simulations show that this peak becomes reduced when the calculations are performed for a tilted detector mirror, which is the more realistic detection set-up [64].

The good agreement between the first-principles-based and measured THz emission spectra ascertains that our modeling provides an adequate description of the spintronic THz emission process. Having established this, we consider in the following how the THz emission can be optimized. If not stated otherwise, we use completely reflective boundaries at the outer interfaces of the emitter. In the following, we focus on how the THz emission from a typical Co/Pt bilayer can be optimized. In Appendix A we provide calculated results for Fe/Pt and Ni/Pt emitters, using the internal FM/NM reflection coefficients reported in Ref. [58].

#### B. Simulated results for FM/NM bilayers

The FM/NM bilayer system is considered as the fundamental element of THz spin-based technologies [8, 15, 19, 61, 70–72]. In what follows, we assume that the laser always excites the sample from the ferromagnetic side, as depicted in Fig. 1.

The aspects of the setup that can influence the shape and characteristics of the spin current and, therefore, the emitted THz emission, can be divided into two categories: passive and active characteristics. In the passive category, we place those elements which we cannot vary from experiment to experiment using the same sample. These

are the physical properties of the experimental setup, i.e., the specific materials composing the multi-layered heterostructure, the quality of the interfaces, the number of layers and their thicknesses. In the active category, we place those elements that are not intrinsic to the setup and can be engineered at will. These include the properties of the laser pulse exciting the sample, which can be the pulse length, the number of pulses, and the intensity. In the following considerations, we will not include the influence of the electro-optic detector crystal. Such detector crystal is always present in the measurements, but different materials are being used (GaAs, ZnTe, etc.) and with varying thicknesses, which makes the recorded THz spectra setup dependent. Our focus is thus on the THz emission before it is measured with the electro-optic crystal.

To characterize the property of the emitted THz signal, we consider two figures of merit extracted from the frequency profile of the emitted electric field  $E(\nu)$ . The first one is the peak frequency  $\nu_{\max}$ , which is the frequency of the maximum of  $E(\nu)$ . The second one is the signal bandwidth, which we define as the frequency interval in which the signal is reduced by one order of magnitude with respect to the maximum  $E(\nu_{\max})$ . A further quantity that can serve as an indicator is the total integrated power of the emitted radiation,

$$P \propto \int_0^\infty d\nu |E(\nu)|^2, \quad (6)$$

which gives a reasonable measure for the amplitude of the generated THz radiation.

### C. Influence of laser-pulse width

We start our analysis by exploring the effects of the laser-pulse properties on the THz spectrum. Figure 3(a) shows how the simulated signal bandwidth of a Co(2)/Pt(4) bilayer varies with the pump-pulse length, defined as the full width at half maximum (FWHM) of the pulse. When reducing the pump-pulse duration, we observe an increase of the bandwidth in Fig. 3(b). Such bandwidth increase was noted previously by Nenno *et al.* [32]. This effect is to be expected since the emission dynamics is triggered by the laser pulse, i.e., the pump-pulse duration sets the time-scale during which electrons are excited to above the Fermi energy [32]. For a short pump pulse, the emission is strongly dominated by the fast dynamics of the excited hot electrons. These start to act as a signal source as soon as they reach the non-magnetic layer. Therefore, the resulting THz spectrum is more strongly characterized by high-frequency components.

Interestingly, we observe that the peak frequency of the signal is nearly not affected by the change in pulse duration. As we will show in the following sections, it appears instead that the peak frequency of the signal

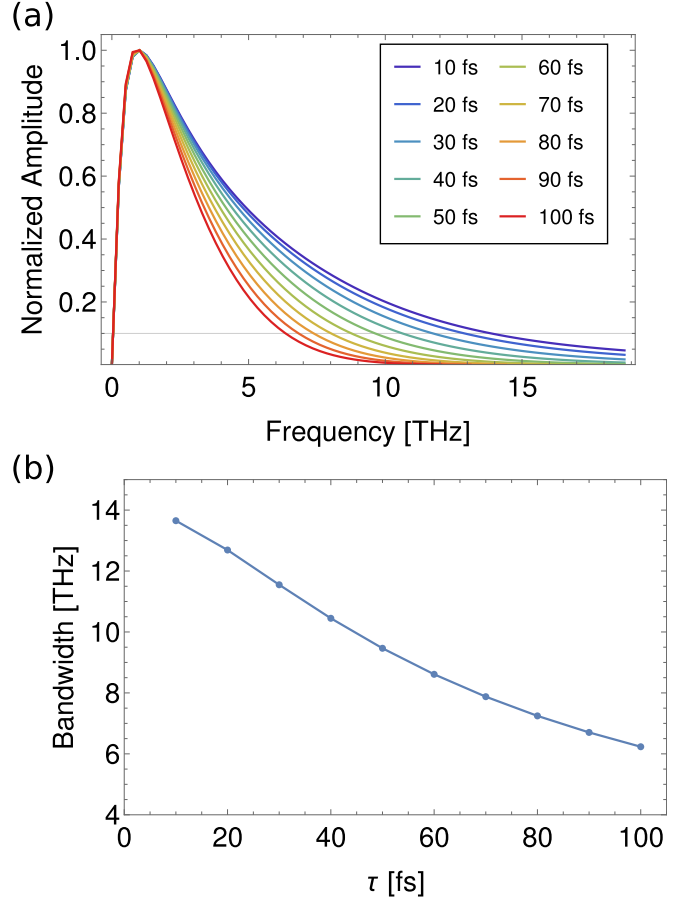


FIG. 3. Results of THz emission calculations. (a) THz emission spectrum of a Co(2)/Pt(4) bilayer computed for different pump durations. (b) Computed THz bandwidth as a function of the femtosecond pump pulse duration.

changes when the geometry of the sample, i.e., layers' thickness and interface properties, is altered. The minor dependence of the peak frequency on the pulse duration is consistent with the expectation that during long pulses hot spin-polarized electrons are injected into the NM material for a longer time, thus resulting in a spectrum peaked at a lower frequency.

Finally, we mention that no effect is instead observed on the bandwidth when the intensity of the laser pulse is changed. The only observed effect is a change in the height of the emission peak, but the time profile of the spin current remains unaffected. This holds within moderate variations of the intensity, in the linear regime of excitation (not complete demagnetization), where the generated spin current scales linearly with the adsorbed laser fluence.

### D. Influence of layer thicknesses

We continue our analysis by exploring the effect of the system size on the THz emission spectrum. In the fol-

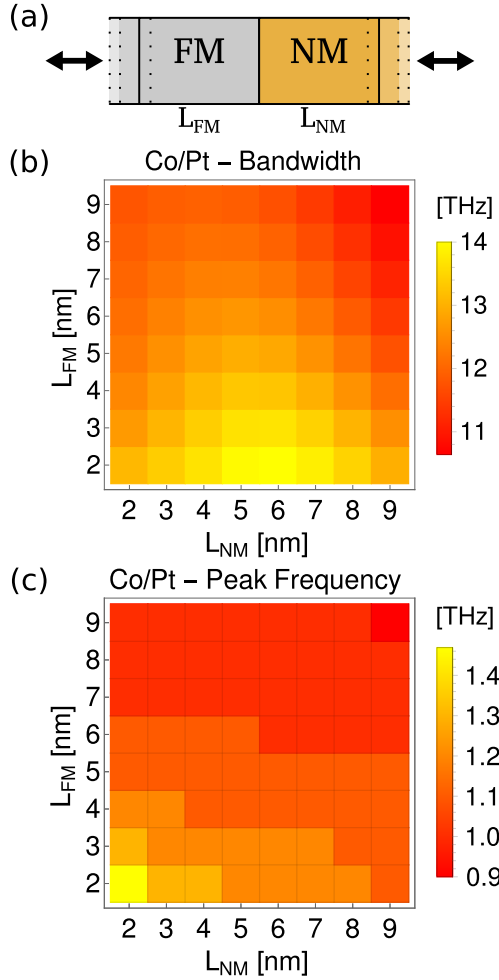


FIG. 4. (a) Schematic representation of the variation of layer thicknesses of the spintronic THz emitter. The thicknesses  $L_{FM}$  of the FM and  $L_{NM}$  of the NM layer are varied independently to study their influence on the THz properties of the system. (b) Simulated THz bandwidth and (c) peak frequency of a  $\text{Co}(L_{FM})/\text{Pt}(L_{NM})$  emitter as a function of the ferromagnetic and nonmagnetic layer thicknesses,  $L_{FM}$  and  $L_{NM}$ , respectively. The grid in the peak frequency plot has been added for better visualization.

lowing calculations, we set the pump-pulse duration to be  $\tau_{\text{pulse}} = 10$  fs. Figures 4(b) and 4(c) show the bandwidth and the peak frequency, respectively, computed as a function of the thickness of the FM layer,  $L_{FM}$ , and the thickness of the NM material,  $L_{NM}$ , schematically shown in Fig. 4(a) for a Co/Pt bilayer. We readily observe how larger layer thicknesses reduce the signal's bandwidth and, at the same time, modify the peak frequency. These findings can be explained by examining the dynamics of the spin current in the superdiffusive model. In the thinner samples, the hot electron wave generated by the fs-laser pulse travels back and forth through the layers before the hot electrons' energies completely decay due to scattering. Consequently, the current profile arises from spin-polarized electrons coming from both sides, de-

structively interfering. This means that the spin current has a short temporal width and, therefore, a large bandwidth. In the thicker sample, the spin current profile is reduced only by the natural decay time, thus appearing as a pulse with a larger spread in time and hence a shorter bandwidth.

Optimal layer thicknesses for a large bandwidth are found to be  $L_{FM} \approx 2 - 3$  nm and  $L_{NM} \approx 5 - 6$  nm. If the Pt thickness is shorter than the Pt diffusion length of about 3 nm [19], hot electrons injected into Pt can easily reach the FM layer again. Here the electrons can be adsorbed in the FM layer due to scattering events and not be injected into the Pt layer a second time, effectively reducing the emission from spin-charge conversion in Pt.

The computed variation of the peak frequency in Fig. 4(c) is relatively small, yet it shows a shift of the peak frequency to lower frequencies with increased Pt thickness. The reason for this behavior is that thicker layers of Pt are favorable for longer-lived excited electron currents, but longer signals result in shorter bandwidths, which correlate well with smaller peak-frequency values. In a thin layer, currents reflect multiple times at the interfaces, interfering destructively and resulting in short-lived signals. In a thicker layer, on the other hand, the current is reflected less often and persists for longer periods of time, comparable to the lifetimes of the excited electrons. This results in a shift to lower peak frequencies for thicker layers.

Together, the competition between the need of a NM layer thin enough that favors destructive interference of the currents but not excessively thin that the electrons are easily injected back in the FM layer, selects the optimal thickness for emission that we observe in Fig. 4(b),(c), which is in overall agreement with experimental results [11, 73].

Another feature that could play a role in the reduction of THz bandwidth from thick Pt layers is the self adsorption in Pt of THz radiation. However, we did not take it into consideration here as the penetration length for THz radiation (of the order of tens of nm) is much larger than the thicknesses in our simulations.

With regard to the materials' dependence, it is worth mentioning that a similar THz emission behavior is obtained, if we use Ni instead of Co for the FM layer, but not for Fe. Details are given in Appendix A. This is due to the unique transport properties, including the interactions with the interfaces, of laser-excited electrons in the three FM metals which result in a different injection of spin-polarized electrons into the NM layer and different secondary injection of back-diffused electrons from the FM into the NM layer.

## E. Interface transmission properties

Besides the thicknesses of the FM and NM layers, the interface between the FM and the NM layer plays a fundamental role, too, in determining the THz emission.

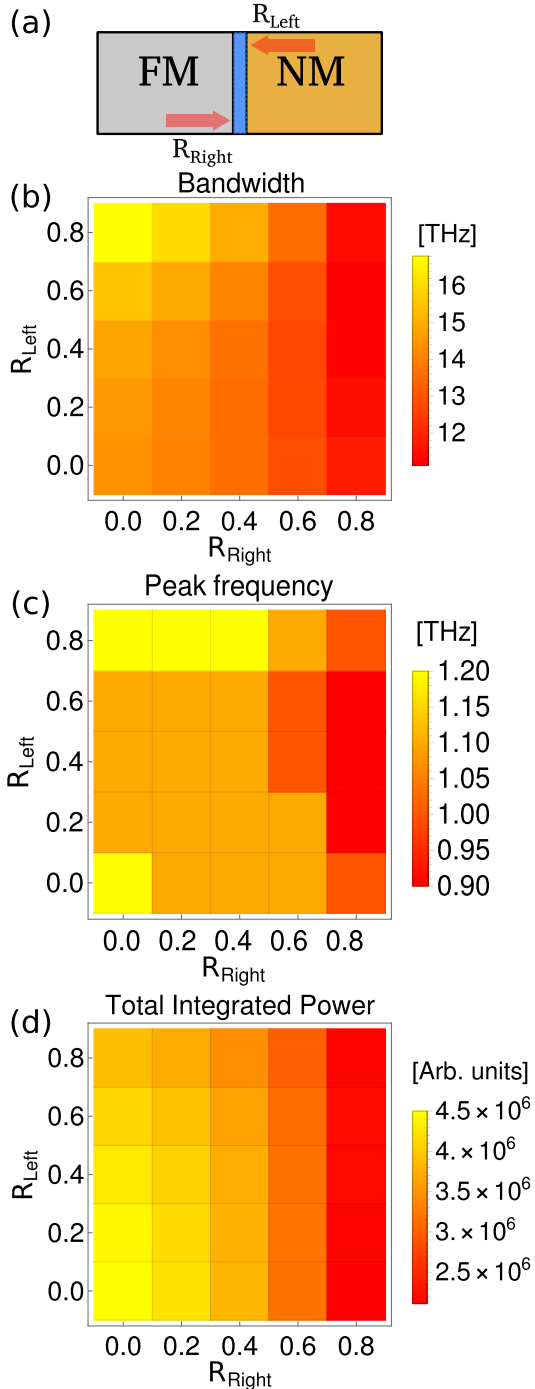


FIG. 5. (a) Schematic illustration of the interface transmission properties of the spintronic emitter. (b) Simulated signal bandwidth, (c) peak frequency, and (d) total integrated THz power as a function of the interface reflection coefficients for left- and right-moving electrons,  $R_{\text{Left}}$  and  $R_{\text{Right}}$ , respectively. The signals are calculated for a Co(2)/Pt(4) bilayer.

The separating region between the two layers contributes in two different ways, depending on the direction of the spin current that crosses this region, see Fig. 5(a). Considering the polarized spin current coming from the FM side and injected in the NM layer (right-moving elec-

trons), it acts as a filter, reducing the amount of current that contributes to the THz emission. On the other side, it acts as a barrier for the spin current flowing from the NM part of the emitter (left-moving electrons), preventing it from being diffused again into the FM layer, thus trapping the electrons in the NM region, where the spin current is converted in charge current due to ISHE.

In Fig. 5(b) we show the computed bandwidth for different values of the interface reflection coefficients in an Co(2)/Pt(4) bilayer. For simplicity, we assume the reflection coefficients at the interface to be independent of the electrons' energy, and the interfaces with the outside of the emitter to be perfectly reflecting ( $R=1$ ). For comparison, the energy-dependent reflection coefficients are reported in Appendix C. The case with perfectly adsorbing external interfaces ( $R=0$ ) is discussed in Appendix B. We study the variation of the bandwidth for different values of the reflection coefficients with respect to right-moving ( $R_{\text{Right}}$ ) and left-moving ( $R_{\text{Left}}$ ) electrons. We observe that a maximum bandwidth is obtained for high values of  $R_{\text{Left}}$ , meaning that the electrons coming from the NM layer are mostly reflected back and constrained within the NM layer, giving a higher contribution to the emission than if they were injected back into the FM layer. With respect to the right-moving electrons, the optimal bandwidth is obtained for low reflection coefficients  $R_{\text{Right}}$ , meaning that the preferred configuration is one that favors electrons' injection from the FM into the NM layer, giving again a positive contribution to the spin current in the NM layer that further increases the THz emission signal.

It is furthermore interesting to analyze how the total integrated power is affected by the changes of the reflection coefficients at the interface. We observe in Fig. 5 that the maximum integrated power is obtained for low values of the  $R_{\text{Right}}$  coefficient, meaning that a more "transparent" interface is ideal for a high integrated power, as electrons can freely diffuse into the NM layer and participate in the THz emission. Comparing with the bandwidth maximum, occurring for high values of  $R_{\text{Left}}$  and low values of  $R_{\text{Right}}$ , the total integrated power for these reflection coefficients is slightly lower. Finally, a minimum integrated power is obtained for high values of  $R_{\text{Right}}$ , which means that very few electrons can pass from the FM into the NM layer, so the emitted electric field is at its lowest in this configuration.

## F. Boundary properties

Next, we move our analysis to focusing on the role of the outer boundaries of the system. In any realistic scenario, the spintronic source will be grown on a substrate or protected with a cap material. Thus, the properties of the boundaries between the bilayer and the external environment, see Fig. 6(a), are expected to impact the shape of the THz spectrum. We can distinguish two extreme cases: when the boundary is completely reflective,

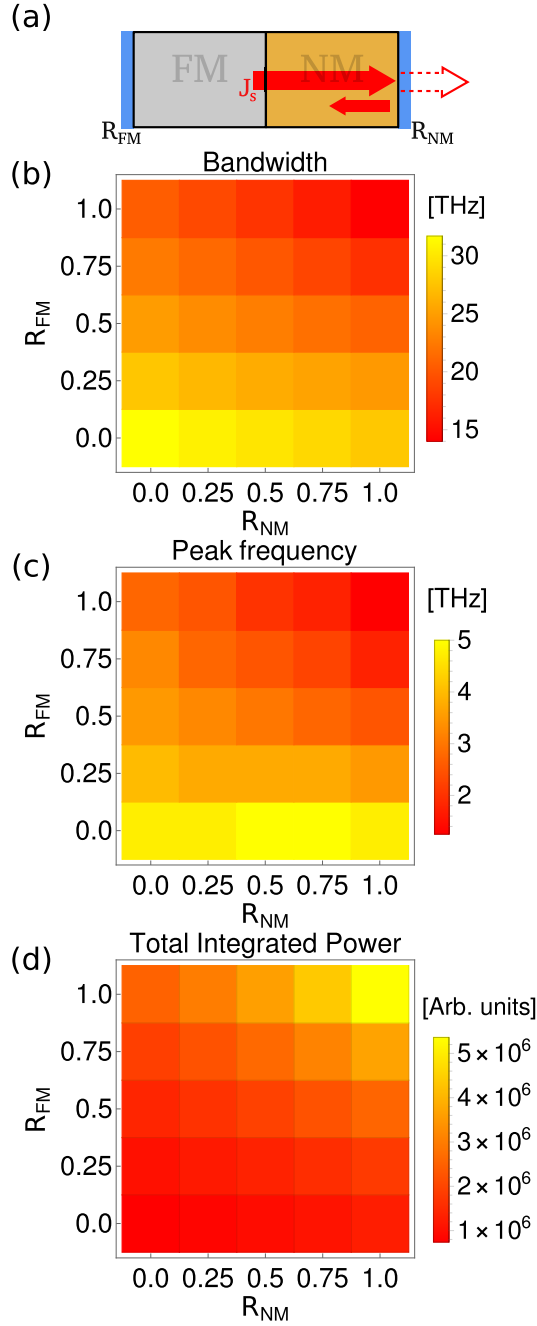


FIG. 6. (a) Schematic illustration of the influence of the outer boundaries of the spintronic THz emitter. (b) Simulated signal bandwidth, (c) peak frequency, and (d) total integrated THz power as a function of the external boundary reflection coefficients for the ferromagnetic and nonmagnetic layers,  $R_{FM}$  and  $R_{NM}$ , respectively. The signals are simulated numerically for a Co(2)/Pt(4) bilayer.

thus the spin current perfectly bounces off the edge and is injected again into the system, and the case in which no component of the spin current is reflected back into the system and the boundary acts as a so-called *spin sink* [19, 74, 75].

In Fig. 6(b)-(d) we show the computed bandwidth, the

peak frequency, and the total integrated power for the Co(2)/Pt(4) bilayer. As in the previous case, the reflection coefficients at the boundary are considered energy independent, while the reflection coefficients at the inner Co-Pt interface have not been changed. We can distinguish some general trends: the bandwidth is larger for lower values of the reflectivity at the boundaries, with a slightly higher bandwidth enhancement for low reflection coefficients at the FM outer boundary; an asymmetry which is related to the nonequal thicknesses of the two layers. We can understand this behavior of the bandwidth further by considering the time scale of the current and the scattered electrons in the two limit cases. For completely adsorbing boundaries ( $R=0$ , i.e., spin sink), the timescale related to the injection of the spin current is only determined by the pulse duration, the hot electrons' speed, and their lifetime. In absence of reflections at the boundaries, the spin current generated in the FM layer propagates through the NM layer and is then evicted from the system, resulting in the shortest possible current, which translates in the largest bandwidth of the emitted signal. On the other hand, as shown in Fig. 6(d), the total emitted power is the lowest in this case, meaning that a great amount of injected energy is lost due to the spin current adsorbing boundaries.

In the case of completely reflecting boundaries ( $R=1$ ) however, there are two consecutive contributions to the signal: the hot electrons that reach the NM layer right after being excited, as well as a portion of electrons which first scatter off the outer boundary surface before reaching the NM material and are injected in the NM layer at later times. This results in a longer spin-current dynamics, which translates into a smaller spectral bandwidth. The integrated power is maximum in this case, up to a factor of five greater than the completely adsorbing boundaries, as there is no loss of hot electron energy at the boundaries.

Moving forward, we observe an interesting pattern in the peak frequency, Fig. 6(c). The peak frequency is larger for lower reflectivity at the FM outer boundary, similar to the trend seen in the bandwidth. Relatively large peak frequencies are still possible in the presence of moderate reflection (up to  $R_{NM} = 0.5$ ) at the NM layer. The peak frequency reaches its minimum when both the external boundaries are completely reflective. This behavior can be explained using similar arguments as for the signal bandwidth. When the external boundary of the NM material is completely reflective, the generated spin current is long lived, and the resulting THz signal has significant low-frequency contributions. Conversely, in the spin-sink case, the currents in the system are quick and short-lived, resulting in signals with more pronounced higher frequency components.

### G. Double pump-pulse emitters

Lastly, to achieve even larger bandwidths, we consider an alternative setup for a spintronic emitter, a trilayer excited by two pump-laser pulses. Figure 7(a) shows such trilayer spintronic emitter, where the two outer layers are composed of a FM material, and the central layer is the heavy NM material that generates the charge current and is responsible for the THz emission. This configuration is distinct from commonly-used trilayer emitters, wherein the central FM layer is sandwiched between two NM layers of opposite spin Hall angle, typically W and Pt [11, 76, 77]. In our different configuration, two separate laser pulses excite the emitter from both sides, resulting in two spin currents that originate in either one of the FM layers.

In particular, the choice of thin FM layers favors a well-defined propagation direction of the excited spin currents. When a laser pulse excites a metal, the hot electrons can travel in all directions with the same probability; however, if we consider a thin layer, electrons that travel toward the outer boundary will immediately scatter at the outside interface and be reflected, reverting their direction (we are considering the case of perfectly reflecting boundary conditions, but a spin sink would just adsorb electrons traveling in one direction and produce similar results), thus resulting in an excited spin current that flows mostly in the direction of the interface with the NM material.

By exciting with two laser pulses with a certain delay  $\Delta t$ , the two opposite-traveling spin-polarized currents will interfere destructively, resulting in a signal being narrower in time and, as such, wider in frequency space. Figure 7(b) shows the THz bandwidth results computed for a Co(2)/Pt(8)/Co(2) trilayer. As this figure reveals, the two-pulses excitation can result in a larger or shorter bandwidth, as compared to the bilayer spintronic emitter, depending on the delay  $\Delta t$  between the two pulses and the pump pulse duration  $\tau$ . If the delay between the laser pulses is too short or too long, then the resulting spin currents do not interfere in an optimal way. The time-delayed second spin current  $J_s(t + \Delta t)$  should cancel the tail of the first spin current  $J_s(t)$  (cf. [64]) to produce a resulting signal more confined in time, according to  $J_s(t) - J_s(t + \Delta t) \approx -\Delta t dJ_s(t)/dt$ . For a delay of the order of the FWHM of the initial pulse, we obtain the maximum value of the bandwidth, see Fig. 7(c).

As shown in Sec. III E, the properties of the THz emission are strongly dependent on the geometry of the emitter. Hence, a comparison between a trilayer and a bilayer spintronic emitter must be discussed carefully. In the bilayer case we found an optimal geometry in the Co(2)/Pt(5-6) bilayer to achieve the largest emission, but this is not the case for a trilayer. Comparing different configurations of various thickness  $x$  of the Pt layer, i.e., Co(2)/Pt( $x$ )/Co(2) (with  $x$  ranging from 4 to 14 nm) we found that the largest bandwidth corresponds to somewhat thicker platinum layers, of about 8 nm, contrary to

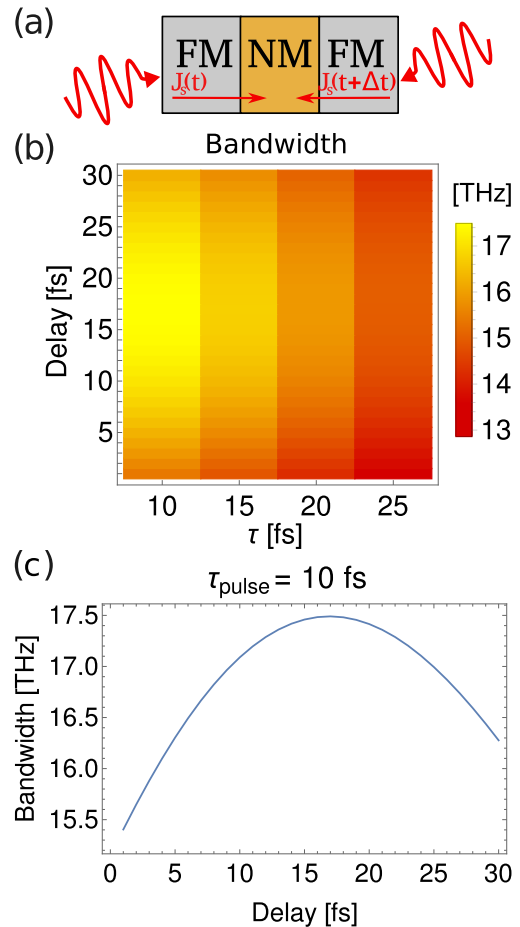


FIG. 7. (a) Schematic representation of the two pump-pulses setup. The FM/NM/FM trilayer is excited from both sides by two time-delayed laser pulses. The resulting spin currents move in opposite directions and can interfere with each other while propagating in the system. (b) Computed THz bandwidth as a function of the laser pulses' FWHM  $\tau$  and time delay  $\Delta t$  between the two exciting pulses, for an Co(2)/Pt(8)/Co(2) spintronic trilayer emitter. (c) Computed THz signal bandwidth as function of the time delay  $\Delta t$  for  $\tau = 10$  fs.

the bilayer case.

In Fig. 7(c) we report the results for a Co(2)/Pt(8)/Co(2) trilayer, and not for the thickest Pt layer we considered. For Pt thicknesses larger than 8 nm, the bandwidth remains practically constant. Hence, we consider the 8 nm layer more interesting as it is the thinnest layer that results in a larger bandwidth than the one of the best bilayer, Co(2)/Pt(6), as reported in Fig. 4. It should additionally be noted that there is a trade-off between the bandwidth and the amplitude of the emitted radiation. Depending on the time delay between the two pulses, the temporal squeezing of the spin current can reduce its amplitude, which in turn leads to a smaller peak amplitude.

#### IV. DISCUSSION AND CONCLUSIONS

Our investigation contributes to the on-going discussion on the physical origin of spintronic THz emission. Several mechanisms and models have been proposed to explain such THz emission. Apart from the superdiffusive spin transport [15, 41, 47], THz emission has been attributed, among others, to the spin Seebeck effect [62, 78, 79], spin voltage [37], spin pumping [35, 80], and spin currents with diffusive [19] and both ballistic and diffusive transport characteristics [81]. Recently, also time-dependent density functional theory (TD-DFT) has been employed to calculate the charge dynamics and resulting THz electric field [38, 66].

Several differences and similarities between these models can be observed. The electron transport in the superdiffusive regime and in TD-DFT calculations is non-thermal, whereas other approaches assume thermalized spin-polarized transport. The direction of the spin  $\sigma$  in the superdiffusive spin current is longitudinal to the moment  $\mathbf{M}$  in the FM layer, i.e.,  $\sigma \parallel \mathbf{M}$ . Also in TD-DFT calculations the reduction of the magnetic moment in the FM layer is longitudinal [38, 66]. The spin direction in the conventional spin pumping mechanism [82] is conversely transverse, i.e.,  $\sigma \parallel (\mathbf{M} \times \partial \mathbf{M} / \partial t)$ , thus,  $\sigma \perp \mathbf{M}$ . An additional conversion step due to spin accumulation at the FM/NM interface has been assumed in Refs. [35, 80] that makes the outgoing spin current longitudinal. This longitudinal nature of the spin current is consistent with direction-sensitive magneto-optical measurements [48, 49, 51, 83]. Further, superdiffusive spin transport contains simultaneously electrons that have not scattered much during the first tens of fs and are moving nearly ballistically, as well as electrons that have undergone many scatterings and propagate in the diffusive regime [41]. Due to the electron scatterings the amount of ballistic electrons decays with time after the laser excitation. A combination of ballistic and diffusive spin transport [81] can provide a reasonable approximation to this process at a certain time. An asset of the superdiffusive transport model is furthermore that it is based on *ab initio* calculated materials' specific quantities. Ultimately, however, the comparison with experiment should resolve what the most applicable model to describe spintronic THz emission is.

In this work, we have systematically explored the spectral features of the THz spectrum when ultrafast spin currents, as computed by the superdiffusive spin-transport model, are taken as source terms for the emitted electric field. In our modeling, we take into account the energy dependence of the spin Hall effect in Pt, thus effectively accounting for the stronger contribution of hot electrons with energies below 0.5 eV, whereas higher-energy electrons with a low value of the spin Hall conductivity do not contribute directly, but only after scattering and losing energy to populate energy levels with higher spin Hall conductivity.

Considering a Co/Pt THz emitter as a typical test case,

we obtain very good agreement between numerical simulations and experimental data for a Co(2)/Pt(4) bilayer, see Fig. 2. Both the THz emission peak and the THz bandwidth are correctly predicted, which supports that the here-proposed modeling provides a suitable description of the ultrafast spin current processes leading to the spintronic THz emission.

Having achieved good agreement between our simulations and experiment, we have aimed to identify optimal conditions to maximize the THz emission. To this end, we have explored numerically the effect of different pulse durations, the influence of the relative thicknesses of the two composing materials, the role of the reflecting or transmitting properties of the FM/NM interface, as well as of the cap and substrate layers. In addition, we have proposed and simulated a trilayer emitter in a double pulse setup.

To summarize, our simulations show specifically, first, that shorter excitation pulses are favorable to reach larger bandwidths and higher values of the peak emission frequency. Second, our simulations show that a thin heavy-metal layer (5–6 nm) provides a sizable bandwidth and good peak emission frequency as compared to thicker nonmagnetic NM layers. Similarly, thin FM layers (2–3 nm) are predicted to provide good THz pulse bandwidths and peak frequencies. Third, investigating the transmission properties of the FM/NM interface we find that, for obtaining a large bandwidth, the interface should optimally act as a filter with a high transmissivity of a hot electrons injected into the NM layer, but with a low transmission of hot electrons flowing back into the FM layer, so that electrons are confined longer in the NM side of the emitter. Fourth, modeling the transmission/reflection at external boundaries of bilayer THz emitters, we find that larger bandwidths and higher emission frequencies are expected for reduced reflections at the boundaries, i.e., for spin sinks, however, with a trade off for the emitted power or the maximum amplitude of the generated signal being reduced. Finally, we have proposed an alternative way to increase the bandwidth of the emitted signal by using a double-pulse setup that could become a versatile tool in actively tuning the emitted electric field while leaving the emitter itself unchanged. The here-predicted THz emitter properties can be examined in dedicated experiments, which will further contribute to establishing rigorously the disputed mechanisms that lead to THz electric field emission.

#### ACKNOWLEDGMENTS

This work has been supported by the Swedish Research Council (VR), the German Research Foundation (Deutsche Forschungsgemeinschaft) through CRC/TRR 227 “Ultrafast Spin Dynamics” (project MF, project-ID: 328545488), the K. and A. Wallenberg Foundation (Grants No. 2022.0079 and 2023.0336), the French National Research Agency PEPR SPIN ANR-22 EXSP-

0003 “TOAST”, and French National Research Agency (ANR) under ANR-21-CE24-0011 “TRAPiST”. This work was further supported by the European Union’s Horizon 2020 Research and Innovation Programme under FET-OPEN Grant Agreements No. 863155 (s-Nebula) and 964735 (EXTREME-IR). The computational resources were provided by the National Academic Infrastructure for Supercomputing in Sweden (NAISSL) at NSC Linköping, partially funded by VR through Grant Agreement No. 2022-06725.

### Appendix A: Influence of layer thicknesses for Co/Pt, Fe/Pt and Ni/Pt

Here we report additional results for the simulated THz emission of Co/Pt, Fe/Pt and Ni/Pt bilayers. In Fig. 8 we show the calculated bandwidth, peak frequency, and total integrated power, respectively, as a function of the layer thicknesses  $L_{NM}$  and  $L_{FM}$ . As in Fig. 4, we set the boundary reflection coefficients at 0.95 when computing the peak frequency. Qualitatively, changing the FM metal of the bilayer does not change dramatically the THz properties of the emitter. We observe for each of the 3d FMs a preference for thin FM layers to achieve a large bandwidth, together with an intermediate thickness of the Pt layer.

Similar to the Co case, a maximum bandwidth is, for example, obtained for the Ni(2)/Pt(6) bilayer, while Fe seems to perform better with the thinnest Pt layer. The dependence of the peak frequency on the emitter thickness is weak for each of the 3d FMs, and also the total integrated power is qualitatively the same. It is worth noting that a higher integrated power is obtained for thicker FM layers, because these lead to a greater demagnetization current and a higher injection of spin-polarized electrons into the NM layer.

### Appendix B: Interface effects combined with nonreflective boundaries

In Sec. III E we considered the influence of reflection and transmission at the FM/NM interface, in combination with fully reflective outer boundaries, i.e.,  $R_{FM} = R_{NM} = 1$ , typical for a spintronic emitter on an insulator substrate. Here we report additional simulations for an Co(2)/Pt(4) emitter with nonreflective outer boundaries. Figure 9 shows the computed THz signals when we consider the outer boundaries to be completely transparent, i.e.,  $R = 0$ , a hot electron and spin sink. Thus, the electrons that reach the outer boundaries escape the system. Under this condition we observe that the most important quantity is the reflection coefficient  $R_{Right}$  which acts as a filter for the electrons being injected into the NM layer. The lower the value of  $R_{Right}$ , the higher is the number of injected electrons contributing to the emission and, as

a consequence, the higher is the bandwidth, peak frequency, and total integrated THz power.

The results are quite different from Fig. 5. In Fig. 9 the dependence of the bandwidth and peak frequency on  $R_{Right}$ , which is related to the probability of right-moving electrons to be reflected at the Co/Pt interface, is rather weak and these THz quantities are much more sensitive to changes of  $R_{Left}$ . conversely, the total integrated power is found to be mostly independent of  $R_{Left}$  and more sensitive to changes in  $R_{Right}$ .

We mention however that the total change in bandwidth, when varying the reflection coefficients, of approximately few THz, is relatively small when compared with a bandwidth of the order of 30 THz. The explanation of this behavior is that, for transparent outer boundaries, there are no electrons reflected at the outer boundary of the NM(FM) layer and thus the left-(right-)moving current is almost non-existent, with the exception of a limited number of electrons that are randomly reflected back from inside the thin Pt(Co) layer. Hence, the effect of  $R_{Left}$  ( $R_{Right}$ ) is negligible when the outer boundaries act as a perfect spin sink ( $R_{Boundary} = 0$ ).

Next, we consider the influence of different reflection/transmission coefficients for spin majority and minority electrons. Recent *ab initio* calculations have shown that such difference can be expected to occur [19, 47]. We consider the Co(2)/Pt(4) bilayer and assume that the reflection coefficients for left and right-moving electrons are the same, i.e.,  $R = R_{Left} = R_{Right}$  and we do not include an energy dependence of the reflection coefficient, but we assume different reflection coefficients for spin up ( $R_{Up}$ ) and spin down ( $R_{Down}$ ). The calculated result for the effect of spin-dependent reflection coefficients on the THz bandwidth is shown in Fig. 10. One can straightforwardly observe that the maximum of the bandwidth is obtained for a low reflection of the spin-up electrons, while the reflective properties of the interface for the spin-down electrons has only a minor influence on the bandwidth. This highlights how the majority spin carriers injected from the FM give the biggest contribution to the THz emission.

We note additionally that the results of the spin sink and interface dependent configurations (cf. Figs. 5, 9 and 10) do not depend strongly on the choice of FM metal. We performed the calculations with Fe and Ni instead of Co and, aside from different bandwidth values, the qualitative behavior is the same.

Lastly, we return to the energy dependence of the reflection/transmission at the FM/NM interface. The reflection of hot electrons at the interface can depend on the energy of the hot electrons, a situation which, according to *ab initio* calculations, frequently occurs [19, 47, 58]. In Fig. 5 we showed the computed bandwidth for different values of the interface reflection coefficients in an Co(2)/Pt(4) bilayer. In the following we investigate further the influence of the energy-dependent reflectivity coefficient.

To this end, we change the reflection coefficients in an

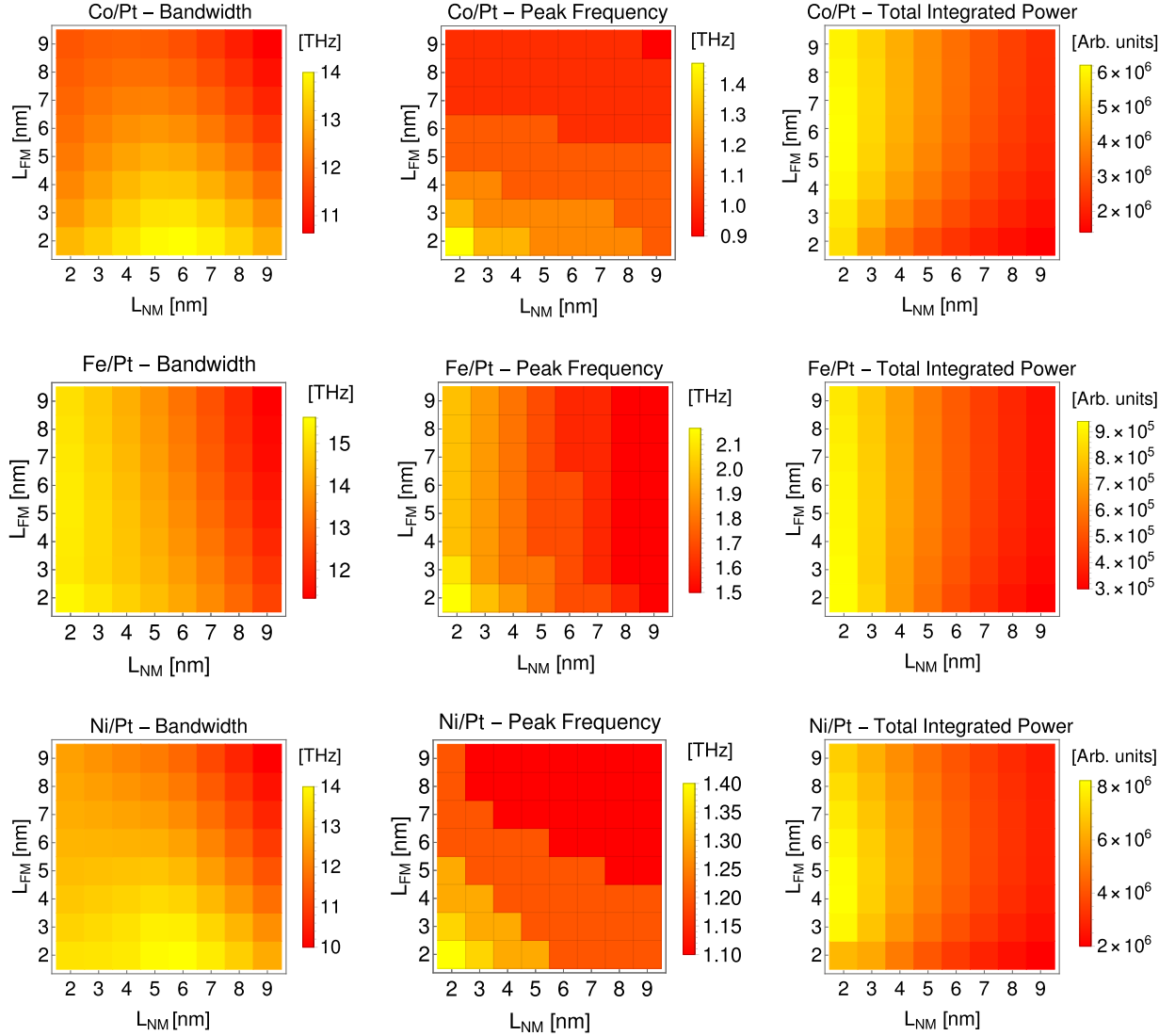


FIG. 8. Calculated THz signal bandwidth (left), THz peak frequency (center), and total integrated power of the emitted radiation (right), plotted as a function of the FM and NM layer thicknesses,  $L_{FM}$  and  $L_{NM}$ . The THz emission properties are calculated for a Co/Pt (top row), Fe/Pt (middle row), and Ni/Pt (bottom row) bilayer, respectively.

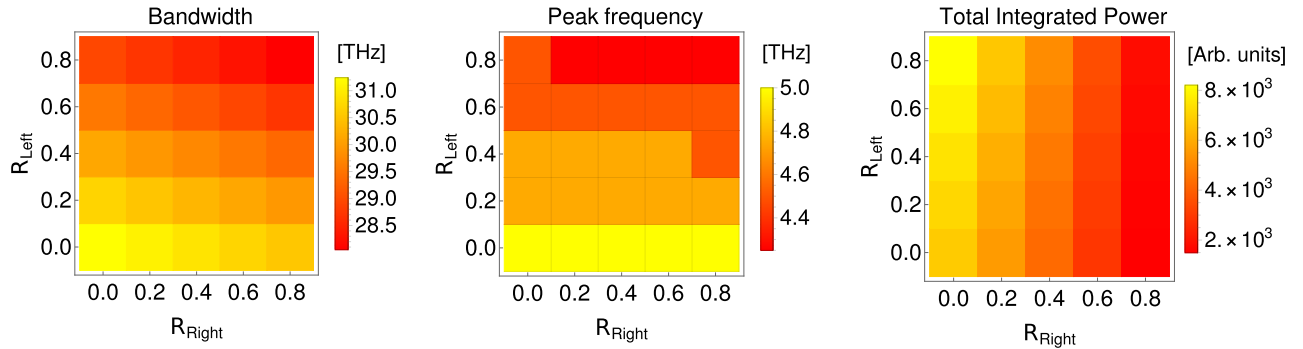


FIG. 9. Simulated THz signal bandwidth, peak frequency, and total integrated THz power as a function of the interface reflection coefficients for left- and right-moving electrons,  $R_{Left}$  and  $R_{Right}$ , respectively. The signals are calculated for an Co(2)/Pt(4) bilayer with perfectly transparent outer boundaries ( $R = 0$ ), i.e., the outer layers act as a hot electron spin sink.

energy-dependent fashion. As the reflection coefficients must only assume values between 0 and 1, it is usually

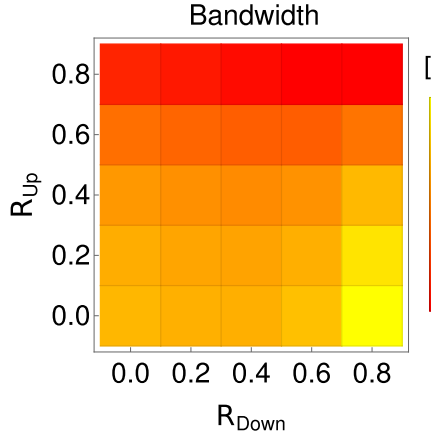


FIG. 10. Simulated bandwidth of an Co(2)/Pt(4) spintronic emitter as a function of the Co/Pt interface reflection coefficients for spin up ( $R_{Up}$ ) and spin down ( $R_{Down}$ ) electrons. The reflection coefficients are assumed to be independent of the electrons' energy.

not possible to increase, or decrease, uniformly the different coefficients at different energies without exceeding the interval  $[0, 1]$ . Hence, to increase, or decrease, the reflection coefficient in a way that maintains the energy-dependent character of the coefficients we define the following quantities:

$$\begin{aligned} R_{\text{decr}}(E) &= R(E) - \alpha R(E), \\ R_{\text{incr}}(E) &= R(E) + \beta(1 - R(E)), \end{aligned} \quad (\text{B1})$$

where  $\alpha$  and  $\beta$  can be seen to decrease and increase, respectively, the reflectivity, and are both positive and smaller than 1. It follows that  $R_{\text{decr}}$  is smaller or equal to  $R(E)$ , but never negative, as well as  $R_{\text{incr}}$  is always greater or equal to  $R(E)$ , but never exceeds 1. By using  $R_{\text{decr}}(E)$  or  $R_{\text{incr}}(E)$  instead of the usual  $R(E)$  (taken from Ref. [58]), we can study how the bandwidth changes with decreasing (increasing)  $\alpha$  or increasing (decreasing)  $\beta$  values of the interface reflection coefficient. This approach allows to retain the energy-dependent character of the reflection coefficients, but we must be aware that the increase or decrease of the reflection coefficients depends on the energy and on the original values of the coefficients. Figure 11 shows the result of such simulations for the Co(2)/Pt(4) emitter. It can be seen that by reducing the reflection coefficients at the interface (larger  $\alpha$ ) the bandwidth increases, similarly to the uniform case described in the main text. Conversely, as expected, an increase of the reflection coefficient (larger  $\beta$ ) generates a reduction of the bandwidth, further corroborating the results reported in Sec. III E for the simplified case of uniform reflection coefficients. This behavior does not depend on the choice of the FM metal.

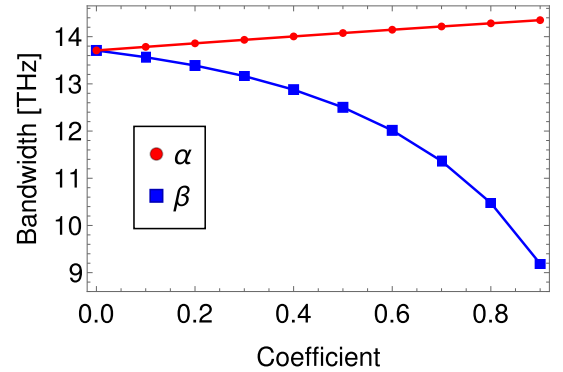


FIG. 11. Calculated variation of the THz bandwidth of a Co(2)/Pt(4) emitter as function of the coefficients  $\alpha$  and  $\beta$ , see Eq. (B1). The values of the interface reflection coefficients  $R(E)$  are reduced, for every value at different energies, for larger coefficient  $\alpha$ , whereas they are increased for larger coefficient  $\beta$ .

### Appendix C: Reflection coefficients

In Fig. 12 we report the reflection coefficients we used in our simulations. The coefficients for Ni/Pt and Fe/Pt interfaces are taken from Ref. [58]. The coefficients for Co/Pt are not available, so we estimated them by averaging the coefficients for Fe/Pt and Ni/Pt.

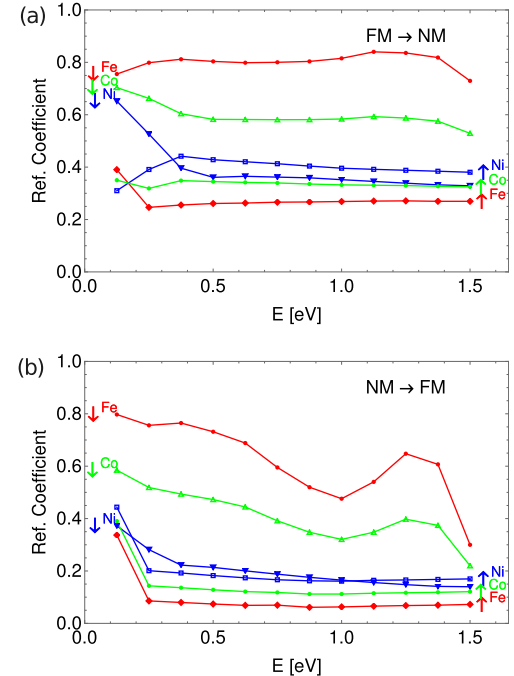


FIG. 12. Reflection coefficients taken from Ref. [58] for Fe/Pt and Ni/Pt interfaces as a function of energy for spin up ( $\uparrow$ ) and down ( $\downarrow$ ) electrons, traveling from the FM to the Pt NM layer (a) and *vice versa* (b). We assume the reflection coefficients for Co/Pt as an average of the coefficients for Fe/Pt and Ni/Pt.

---

[1] Y.-S. Lee, *Principles of terahertz science and technology*, Vol. 170 (Springer Science & Business Media, New York, 2009).

[2] S. L. Dexheimer, *Terahertz Spectroscopy: Principles and Applications* (CRC Press, Boca Raton, 2017).

[3] D. M. Mittleman, Perspective: Terahertz science and technology, *J. Appl. Phys.* **122**, 230901 (2017).

[4] B. Ferguson and X.-C. Zhang, Materials for terahertz science and technology, *Nat. Mater.* **1**, 26 (2002).

[5] M. Tonouchi, Cutting-edge terahertz technology, *Nat. Photon.* **1**, 97 (2007).

[6] S. S. Dhillon, M. S. Vitiello, E. H. Linfield, A. G. Davies, M. C. Hoffmann, J. Booske, C. Paoloni, M. Gensch, P. Weightman, G. P. Williams, E. Castro-Camus, D. R. S. Cumming, F. Simoens, I. Escoria-Carranza, J. Grant, S. Lucyszyn, M. Kuwata-Gonokami, K. Konishi, M. Koch, C. A. Schmuttenmaer, T. L. Cocker, R. Huber, A. G. Markelz, Z. D. Taylor, V. P. Wallace, J. A. Zeitler, J. Sibik, T. M. Korter, B. Ellison, S. Rea, P. Goldsmith, K. B. Cooper, R. Appleby, D. Pardo, P. G. Huggard, V. Krozer, H. Shams, M. Fice, C. Renaud, A. Seeds, A. Stöhr, M. Naftaly, N. Ridler, R. Clarke, J. E. Cunningham, and M. B. Johnston, The 2017 terahertz science and technology roadmap, *J. Phys. D: Applied Phys.* **50**, 043001 (2017).

[7] E. T. Papaioannou and R. Beigang, THz spintronic emitters: a review on achievements and future challenges, *Nanophoton.* **10**, 1243 (2020).

[8] C. Bull, S. M. Hewett, R. Ji, C.-H. Lin, T. Thomson, D. M. Graham, and P. W. Nutter, Spintronic terahertz emitters: Status and prospects from a materials perspective, *APL Materials* **9**, 090701 (2021).

[9] A. Nahata, A. S. Weling, and T. F. Heinz, A wideband coherent terahertz spectroscopy system using optical rectification and electro-optic sampling, *Appl. Phys. Lett.* **69**, 2321 (1996).

[10] N. M. Burford and M. O. El-Shenawee, Review of terahertz photoconductive antenna technology, *Opt. Engineering* **56**, 010901 (2017).

[11] T. Seifert, S. Jaiswal, U. Martens, J. Hannegan, L. Braun, P. Maldonado, F. Freimuth, A. Kronenberg, J. Henrizi, I. Radu, E. Beaurepaire, Y. Mokrousov, P. M. Oppeneer, M. Jourdan, G. Jakob, D. Turchinovich, L. M. Hayden, M. Wolf, M. Münzenberg, M. Kläui, and T. Kampfrath, Efficient metallic spintronic emitters of ultrabroadband terahertz radiation, *Nat. Photon.* **10**, 483 (2016).

[12] M. Chen, Y. Wu, Y. Liu, K. Lee, X. Qiu, P. He, J. Yu, and H. Yang, Current-Enhanced Broadband THz Emission from Spintronic Devices, *Adv. Optical Mater.* **7**, 1801608 (2019).

[13] R. Adam, G. Chen, D. E. Bürgler, T. Shou, I. Komissarov, S. Heidtfeld, H. Hardtdegen, M. Mikulics, C. M. Schneider, and R. Sobolewski, Magnetically and optically tunable terahertz radiation from Ta/NiFe/Pt spintronic nanolayers generated by femtosecond laser pulses, *Appl. Phys. Lett.* **114**, 212405 (2019).

[14] W. Wu, C. Yaw Ameyaw, M. F. Doty, and M. B. Jungfleisch, Principles of spintronic THz emitters, *J. Appl. Phys.* **130**, 091101 (2021).

[15] T. Kampfrath, M. Battiato, P. Maldonado, G. Eilers, J. Nötzold, S. Mährlein, V. Zbarsky, F. Freimuth, Y. Mokrousov, S. Blügel, M. Wolf, I. Radu, P. M. Oppeneer, and M. Münzenberg, Terahertz spin current pulses controlled by magnetic heterostructures, *Nat. Nanotechnol.* **8**, 256 (2013).

[16] T. S. Seifert, L. Cheng, Z. Wei, T. Kampfrath, and J. Qi, Spintronic sources of ultrashort terahertz electromagnetic pulses, *Appl. Phys. Lett.* **120**, 180401 (2022).

[17] O. Panahi, B. Yahyaei, S. M. Mousavi, and A. M. Ghiasabadi, High performance terahertz emitter based on inverse spin Hall effect in metallic Fe/Au heterostructure, *Laser Phys.* **30**, 055001 (2020).

[18] M. Yang, K. Cai, H. Ju, K. W. Edmonds, G. Yang, S. Liu, B. Li, B. Zhang, Y. Sheng, S. Wang, Y. Ji, and K. Wang, Spin-orbit torque in Pt/CoNiCo/Pt symmetric devices, *Sci. Rep.* **6**, 20778 (2016).

[19] T. H. Dang, J. Hawecker, E. Rongione, G. Baez Flores, D. Q. To, J. C. Rojas-Sanchez, H. Nong, J. Mangeney, J. Tignon, F. Godel, S. Collin, P. Seneor, M. Bibes, A. Fert, M. Anane, J.-M. George, L. Vila, M. Cosset-Cheneau, D. Dolfi, R. Lebrun, P. Bortolotti, K. Beleshchenko, S. Dhillon, and H. Jaffrès, Ultrafast spin-currents and charge conversion at 3d-5d interfaces probed by time-domain terahertz spectroscopy, *Appl. Phys. Rev.* **7**, 041409 (2020).

[20] W. Zhang, P. Maldonado, Z. Jin, T. S. Seifert, J. Arabski, G. Schmerber, E. Beaurepaire, M. Bonn, T. Kampfrath, P. M. Oppeneer, and D. Turchinovich, Ultrafast terahertz magnetometry, *Nat. Commun.* **11**, 4247 (2020).

[21] M. I. D'yakonov and V. I. Perel', Possibility of orienting electron spins with current, *JETP Lett.* **13**, 467 (1971).

[22] J. E. Hirsch, Spin Hall effect, *Phys. Rev. Lett.* **83**, 1834 (1999).

[23] J. Sinova, S. O. Valenzuela, J. Wunderlich, C. H. Back, and T. Jungwirth, Spin Hall effects, *Rev. Mod. Phys.* **87**, 1213 (2015).

[24] Y. A. Bychkov and E. I. Rashba, Properties of a 2D electron gas with lifted spectral degeneracy, *JETP Lett.* **39**, 78 (1984).

[25] V. M. Edelstein, Spin polarization of conduction electrons induced by electric current in two-dimensional asymmetric electron systems, *Solid State Commun.* **73**, 233 (1990).

[26] M. B. Jungfleisch, Q. Zhang, W. Zhang, J. E. Pearson, R. D. Schaller, H. Wen, and A. Hoffmann, Control of terahertz emission by ultrafast spin-charge current conversion at Rashba interfaces, *Phys. Rev. Lett.* **120**, 207207 (2018).

[27] C. Zhou, Y. P. Liu, Z. Wang, S. J. Ma, M. W. Jia, R. Q. Wu, L. Zhou, W. Zhang, M. K. Liu, Y. Z. Wu, and J. Qi, Broadband Terahertz Generation via the Interface Inverse Rashba-Edelstein Effect, *Phys. Rev. Lett.* **121**, 086801 (2018).

[28] E. Rongione, L. Baringthon, D. She, G. Patriarche, R. Lebrun, A. Lemaître, M. Morassi, N. Reyren, M. Mičica, J. Mangeney, J. Tignon, F. Bertran, S. Dhillon, P. Le Févre, H. Jaffrès, and J.-M. George, Spin-Momentum Locking and Ultrafast Spin-Charge Conversion in Ultrathin Epitaxial  $\text{Bi}_{1-x}\text{Sb}_x$  Topological Insulator, *Adv. Science* **10**, 2301124 (2023).

[29] E. Beaurepaire, G. M. Turner, S. M. Harrel, M. C. Beard, J.-Y. Bigot, and C. A. Schmuttenmaer, Coherent terahertz emission from ferromagnetic films excited by femtosecond laser pulses, *Appl. Phys. Lett.* **84**, 3465 (2004).

[30] D. J. Hilton, R. P. Prasankumar, S. A. Trugman, A. J. Taylor, and R. D. Averitt, On Photo-Induced Phenomena in Complex Materials: Probing Quasiparticle Dynamics using Infrared and Far-Infrared Pulses, *J. Phys. Soc. Jpn.* **75**, 011006 (2006).

[31] T. J. Huisman, R. V. Mikhaylovskiy, J. D. Costa, F. Freimuth, E. Paz, J. Ventura, P. P. Freitas, S. Blügel, Y. Mokrousov, T. Rasing, *et al.*, Femtosecond control of electric currents in metallic ferromagnetic heterostructures, *Nat. Nanotechnol.* **11**, 455 (2016).

[32] D. M. Nenno, R. Binder, and H. C. Schneider, Simulation of hot-carrier dynamics and terahertz emission in laser-excited metallic bilayers, *Phys. Rev. Applied* **11**, 054083 (2019).

[33] J. Pettine, P. Padmanabhan, N. Sirica, R. P. Prasankumar, A. J. Taylor, and H.-T. Chen, Ultrafast terahertz emission from emerging symmetry-broken materials, *Light: Science & Appl.* **12**, 133 (2023).

[34] M. Beens, R. A. Duine, and B. Koopmans, *s-d* model for local and nonlocal spin dynamics in laser-excited magnetic heterostructures, *Phys. Rev. B* **102**, 054442 (2020).

[35] T. Lichtenberg, M. Beens, M. H. Jansen, B. Koopmans, and R. A. Duine, Probing optically induced spin currents using terahertz spin waves in noncollinear magnetic bilayers, *Phys. Rev. B* **105**, 144416 (2022).

[36] G. Schmidt, B. Das-Mohapatra, and E. T. Papaioannou, Charge dynamics in spintronic terahertz emitters, *Phys. Rev. Appl.* **19**, L041001 (2023).

[37] R. Rouzegar, L. Brandt, L. Nádvorník, D. A. Reiss, A. L. Chekhov, O. Gueckstock, C. In, M. Wolf, T. S. Seifert, P. W. Brouwer, G. Woltersdorf, and T. Kampfrath, Laser-induced terahertz spin transport in magnetic nanostructures arises from the same force as ultrafast demagnetization, *Phys. Rev. B* **106**, 144427 (2022).

[38] A. Kefayati and B. K. Nikolić, Origins of Electromagnetic Radiation from Spintronic Terahertz Emitters: A Time-Dependent Density Functional Theory plus Jefimenko Equations Approach, *Phys. Rev. Lett.* **133**, 136704 (2024).

[39] H.-J. Song and T. Nagatsuma, *Handbook of terahertz technologies: devices and applications* (CRC press, Boca Raton, 2015).

[40] S.-C. Chen, Z. Feng, J. Li, W. Tan, L.-H. Du, J. Cai, Y. Ma, K. He, H. Ding, Z.-H. Zhai, Z.-R. Li, C.-W. Qiu, X.-C. Zhang, and L. Zhu, Ghost spintronic THz-emitter-array microscope, *Light: Science & Applications* **9**, 99 (2020).

[41] M. Battiato, K. Carva, and P. M. Oppeneer, Theory of laser-induced ultrafast superdiffusive spin transport in layered heterostructures, *Phys. Rev. B* **86**, 024404 (2012).

[42] A. Eschenlohr, M. Battiato, P. Maldonado, N. Pontius, T. Kachel, K. Holldack, R. Mitzner, A. Föhliisch, P. M. Oppeneer, and C. Stamm, Ultrafast spin transport as key to femtosecond demagnetization, *Nature Mater.* **12**, 332 (2013).

[43] A. Melnikov, I. Razdolski, T. O. Wehling, E. T. Papaioannou, V. Roddatis, P. Fumagalli, O. Aktasipetrov, A. I. Lichtenstein, and U. Bovensiepen, Ultrafast transport of laser-excited spin-polarized carriers in Au/Fe/MgO(001), *Phys. Rev. Lett.* **107**, 076601 (2011).

[44] M. Battiato, K. Carva, and P. M. Oppeneer, Superdiffusive spin transport as a mechanism of ultrafast demagnetization, *Phys. Rev. Lett.* **105**, 027203 (2010).

[45] P. Baláž, M. Žonda, K. Carva, P. Maldonado, and P. M. Oppeneer, Transport theory for femtosecond laser-induced spin-transfer torques, *J. Phys.: Condens. Matter* **30**, 115801 (2018).

[46] W.-T. Lu and Z. Yuan, Spin accumulation and dissipation excited by an ultrafast laser pulse, *Phys. Rev. B* **104**, 214404 (2021).

[47] P. Baláž, M. Zwierzyczyk, F. Cosco, K. Carva, P. Maldonado, and P. M. Oppeneer, Theory of superdiffusive spin transport in noncollinear magnetic multilayers, *Phys. Rev. B* **107**, 174418 (2023).

[48] D. Rudolf, C. La-O-Vorakiat, M. Battiato, R. Adam, J. M. Shaw, E. Turgut, P. Maldonado, S. Mathias, P. Grychtol, H. T. Nembach, T. J. Silva, M. Aeschlimann, H. C. Kapteyn, M. M. Murnane, C. M. Schneider, and P. M. Oppeneer, Ultrafast magnetization enhancement in metallic multilayers driven by superdiffusive spin current, *Nat. Commun.* **3**, 1037 (2012).

[49] M. Hofherr, P. Maldonado, O. Schmitt, M. Berritta, U. Bierbrauer, S. Sadashivaiah, A. J. Schellekens, B. Koopmans, D. Steil, M. Cinchetti, B. Stadtmüller, P. M. Oppeneer, S. Mathias, and M. Aeschlimann, Speed and efficiency of femtosecond spin current injection into a nonmagnetic material, *Phys. Rev. B* **96**, 100403 (2017).

[50] U. Ritzmann, P. Baláž, P. Maldonado, K. Carva, and P. M. Oppeneer, High-frequency magnon excitation due to femtosecond spin-transfer torques, *Phys. Rev. B* **101**, 174427 (2020).

[51] R. Gupta, F. Cosco, R. S. Malik, X. Chen, S. Saha, A. Ghosh, T. Pohlmann, J. R. L. Mardegan, S. Franchoual, R. Stefanuk, J. Söderström, B. Sanyal, O. Karis, P. Svedlindh, P. M. Oppeneer, and R. Knut, Element-resolved evidence of superdiffusive spin current arising from ultrafast demagnetization process, *Phys. Rev. B* **108**, 064427 (2023).

[52] V. P. Zhukov, E. V. Chulkov, and P. M. Echenique, GW+T theory of excited electron lifetimes in metals, *Phys. Rev. B* **72**, 155109 (2005).

[53] V. P. Zhukov, E. V. Chulkov, and P. M. Echenique, Lifetimes and inelastic mean free path of low-energy excited electrons in Fe, Ni, Pt, and Au: Ab initio GW+T calculations, *Phys. Rev. B* **73**, 125105 (2006).

[54] I. A. Nechaev and E. V. Chulkov, Quasiparticle dynamics in ferromagnetic compounds of the Co-Fe and Ni-Fe systems, *Eur. Phys. Jour. B* **77**, 31 (2010).

[55] M. Battiato, P. Maldonado, and P. M. Oppeneer, Treating the effect of interface reflections on superdiffusive spin transport in multilayer samples, *J. Appl. Phys.* **115**, 172611 (2014).

[56] D. M. Nenno, S. Kaltenborn, and H. C. Schneider, Boltzmann transport calculation of collinear spin transport on short timescales, *Phys. Rev. B* **94**, 115102 (2016).

[57] D. M. Nenno, B. Rethfeld, and H. C. Schneider, Particle-in-cell simulation of ultrafast hot-carrier transport in Fe/Au heterostructures, *Phys. Rev. B* **98**, 224416 (2018).

[58] W.-T. Lu, Y. Zhao, M. Battiato, Y. Wu, and Z. Yuan, Interface reflectivity of a superdiffusive spin current in ultrafast demagnetization and terahertz emission, *Phys. Rev. B* **101**, 014435 (2020).

[59] C. Stamm, C. Murer, M. Berritta, J. Feng, M. Gabureac, P. M. Oppeneer, and P. Gambardella, Magneto-Optical

Detection of the Spin Hall Effect in Pt and W Thin Films, *Phys. Rev. Lett.* **119**, 087203 (2017).

[60] L. Salemi and P. M. Oppeneer, First-principles theory of intrinsic spin and orbital Hall and Nernst effects in metallic monoatomic crystals, *Phys. Rev. Mater.* **6**, 095001 (2022).

[61] Y. Wu, M. Elyasi, X. Qiu, M. Chen, Y. Liu, L. Ke, and H. Yang, High-performance thz emitters based on ferromagnetic/nonmagnetic heterostructures, *Adv. Mater.* **29**, 1603031 (2017).

[62] T. S. Seifert, N. M. Tran, O. Gueckstock, S. M. Rouzegar, L. Nadvornik, S. Jaiswal, G. Jakob, V. V. Temnov, M. Münzenberg, M. Wolf, M. Kläui, and T. Kampfrath, Terahertz spectroscopy for all-optical spintronic characterization of the spin-Hall-effect metals Pt, W and Cu<sub>80</sub>Ir<sub>20</sub>, *J. Phys. D: Appl. Phys.* **51**, 364003 (2018).

[63] S. Zhang, Z. Jin, Z. Zhu, W. Zhu, Z. Zhang, G. Ma, and J. Yao, Bursts of efficient terahertz radiation with saturation effect from metal-based ferromagnetic heterostructures, *J. Phys. D: Appl. Phys.* **51**, 034001 (2017).

[64] F. Foggetti and P. M. Oppeneer, Quantitative modeling of spintronic terahertz emission due to ultrafast spin transport, *Phys. Rev. Appl.* **23**, 014067 (2025).

[65] T. J. Huisman, R. V. Mikhaylovskiy, A. Tsukamoto, T. Rasing, and A. V. Kimel, Simultaneous measurements of terahertz emission and magneto-optical kerr effect for resolving ultrafast laser-induced demagnetization dynamics, *Phys. Rev. B* **92**, 104419 (2015).

[66] J. Varela-Manjarres, A. Kefayati, M. B. Jungfleisch, J. Q. Xiao, and B. K. Nikolić, Charge and spin current pumping by ultrafast demagnetization dynamics, *Phys. Rev. B* **110**, L060410 (2024).

[67] O. D. Jefimenko, Solutions of Maxwell's equations for electric and magnetic fields in arbitrary media, *Am. J. Phys.* **60**, 899 (1992).

[68] P. J. Hale, J. Madeo, C. Chin, S. S. Dhillon, J. Mangeney, J. Tignon, and K. M. Dani, 20 THz broadband generation using semi-insulating GaAs interdigitated photoconductive antennas, *Opt. Express* **22**, 26358 (2014).

[69] N. Nilforoushan, T. Apretna, C. Song, T. Boulier, J. Tignon, S. Dhillon, M. Hanna, and J. Mangeney, Generation of Ultra-broadband THz Pulses at a 200 kHz Repetition Rate with Peak Electric Field Above 100 kV/cm, in *2022 47th International Conference on Infrared, Millimeter and Terahertz Waves (IRMMW-THz)* (IEEE, Delft, 2022) pp. 1–1.

[70] E. T. Papaioannou, G. Torosyan, S. Keller, L. Scheuer, M. Battiatto, V. K. Mag-Usara, J. L'huillier, M. Tani, and R. Beigang, Efficient Terahertz Generation Using Fe/Pt Spintronic Emitters Pumped at Different Wavelengths, *IEEE Trans. Magnetics* **54**, 1 (2018).

[71] G. Li, R. Medapalli, R. V. Mikhaylovskiy, F. E. Spada, T. Rasing, E. E. Fullerton, and A. V. Kimel, THz emission from Co/Pt bilayers with varied roughness, crystal structure, and interface intermixing, *Phys. Rev. Mater.* **3**, 084415 (2019).

[72] Z. Feng, H. Qiu, D. Wang, C. Zhang, S. Sun, B. Jin, and W. Tan, Spintronic terahertz emitter, *J. Appl. Phys.* **129**, 010901 (2021).

[73] H. S. Qiu, K. Kato, K. Hirota, N. Sarukura, M. Yoshimura, and M. Nakajima, Layer thickness dependence of the terahertz emission based on spin current in ferromagnetic heterostructures, *Opt. Express* **26**, 15247 (2018).

[74] K. Harii, Z. Qiu, T. Iwashita, Y. Kajiwara, K. Uchida, K. Ando, T. An, Y. Fujikawa, and E. Saitoh, Spin Pumping in a Ferromagnetic/Nonmagnetic/Spin-Sink Trilayer Film: Spin Current Termination, Key Engineering Materials **508**, 266 (2012).

[75] J. Hawecker, E. Rongione, A. Markou, S. Krishnia, F. Godel, S. Collin, R. Lebrun, J. Tignon, J. Mangeney, T. Boulier, J.-M. George, C. Felser, H. Jaffrè, and S. Dhillon, Spintronic THz emitters based on transition metals and semi-metals/Pt multilayers, *Appl. Phys. Lett.* **120**, 122406 (2022).

[76] P. Koleják, G. Lezier, D. Vala, B. Mathmann, L. Halačka, Z. Gelnárová, Y. Dusch, J.-F. Lampin, N. Tiercelin, K. Postava, and M. Vanwolleghem, Maximizing the electromagnetic efficiency of spintronic terahertz emitters, *Adv. Photon. Res.* **5**, 2400064 (2024).

[77] R. Rouzegar, A. Chekhov, Y. Behovits, B. Serrano, M. Syskaki, C. Lambert, D. Engel, U. Martens, M. Münzenberg, M. Wolf, G. Jakob, M. Kläui, T. Seifert, and T. Kampfrath, Broadband spintronic terahertz source with peak electric fields exceeding 1.5 MV/cm, *Phys. Rev. Appl.* **19**, 034018 (2023).

[78] G.-M. Choi, C.-H. Moon, B.-C. Min, K.-J. Lee, and D. G. Cahill, Thermal spin-transfer torque driven by the spin-dependent Seebeck effect in metallic spin-valves, *Nat. Phys.* **11**, 576 (2015).

[79] A. Alekhin, I. Razdolski, N. Ilin, J. P. Meyburg, D. Diesing, V. Roddatis, I. Rungger, M. Stamenova, S. Sanvito, U. Bovensiepen, and A. Melnikov, Femtosecond spin current pulses generated by the nonthermal spin-dependent Seebeck effect and interacting with ferromagnets in spin valves, *Phys. Rev. Lett.* **119**, 017202 (2017).

[80] M. Beens, K. A. de Mare, R. A. Duine, and B. Koopmans, Spin-polarized hot electron transport versus spin pumping mediated by local heating, *J. Phys.: Condens. Matter* **35**, 035803 (2022).

[81] J. Jechumtál, R. Rouzegar, O. Gueckstock, C. Denker, W. Hoppe, Q. Remy, T. S. Seifert, P. Kubačík, G. Woltersdorf, P. W. Brouwer, M. Münzenberg, T. Kampfrath, and L. Nádvorník, Accessing ultrafast spin-transport dynamics in copper using broadband terahertz spectroscopy, *Phys. Rev. Lett.* **132**, 226703 (2024).

[82] Y. Tserkovnyak, A. Brataas, and G. E. W. Bauer, Enhanced Gilbert Damping in Thin Ferromagnetic Films, *Phys. Rev. Lett.* **88**, 117601 (2002).

[83] J. Wieczorek, A. Eschenlohr, B. Weidtmann, M. Rösner, N. Bergeard, A. Tarasevitch, T. O. Wehling, and U. Bovensiepen, Separation of ultrafast spin currents and spin-flip scattering in Co/Cu(001) driven by femtosecond laser excitation employing the complex magneto-optical Kerr effect, *Phys. Rev. B* **92**, 174410 (2015).